AIP | Applied Physics Letters

Detection of filament formation in forming-free resistive switching SrTiO3 devices with Ti top electrodes

S. Stille, Ch. Lenser, R. Dittmann, A. Koehl, I. Krug et al.

Citation: Appl. Phys. Lett. **100**, 223503 (2012); doi: 10.1063/1.4724108
View online: http://dx.doi.org/10.1063/1.4724108
View Table of Contents: http://apl.aip.org/resource/1/APPLAB/v100/i22
Published by the American Institute of Physics.

Detection of filament formation in forming-free resistive switching $SrTiO_3$ devices with Ti top electrodes

S. Stille,[1,a),b)] Ch. Lenser,[2,a),c)] R. Dittmann,[2] A. Koehl,[2] I. Krug,[2] R. Muenstermann,[2] J. Perlich,[3] C. M. Schneider,[2] U. Klemradt,[1] and R. Waser[2,4]
[1]*II. Institute of Physics and JARA-FIT, RWTH Aachen University, D-52056 Aachen, Germany*
[2]*Peter Gruenberg Institute and JARA-FIT, FZ Juelich, D-52425 Juelich, Germany*
[3]*HASYLAB, DESY, D-22607 Hamburg, Germany*
[4]*Institute of Materials in Electrical Engineering and Information Technology II, RWTH Aachen University, D-52056 Aachen, Germany*

(Received 16 February 2012; accepted 14 May 2012; published online 31 May 2012)

We investigated the influence of Ti top electrodes on the resistive switching properties of $SrTiO_3$ thin film devices. Above a Ti layer thickness of 5 nm, the initial resistance is strongly reduced, giving rise to forming-free devices. Hard x-ray photoemission experiments reveal the Ti layer to be composed of several oxide phases, induced by the redox-reaction at the Ti/$SrTiO_3$ interface. Grazing incidence small angle x-ray scattering measurements indicate that the reduction of the $SrTiO_3$ thin film occurs in a filamentary way. We attribute this behavior to the preferential reduction of $SrTiO_3$ thin films along highly defective areas. © *2012 American Institute of Physics*. [http://dx.doi.org/10.1063/1.4724108]

Resistive switching phenomena, which are observed in a large variety of binary and ternary oxides, attract considerable attention due to their high potential as future data storage principle.[1–3] Usually, the oxide-based metal-insulator-metal (MIM) structures are highly insulating in the virgin state and an initial electrical forming process is needed to enable their switching capability or so called memristive behavior.[4] This forming process removes oxygen from the oxide lattice and provides the inevitable amount of donor-type oxygen vacancies to allow sufficient current flow. As a result of electrical stress and Joule heating, electroforming often goes along with dramatic changes of the film morphology, including partial blowoff of electrode material.[5–7] Therefore, increasing efforts are spent in the development of fabricating processes for forming-free devices. Besides the use of special annealing procedures[8] or impurity doping[9] profiles, combinations of reactive electrode materials[10–12] have been reported as promising approaches for the fabrication of forming-free MIM structures. Although a considerable amount of investigations exists about the nanoscale current distribution and filament formation in electroformed devices,[5,6,13] possible device inhomogeneities in forming-free devices have not been studied in detail so far. In this work, we investigated the filament formation in forming-free $SrTiO_3$ MIM structures with Ti top electrodes by employing grazing incidence small angle x-ray scattering (GISAXS). This analysis was complemented by hard x-ray photoemission spectroscopy (HAXPES) in order to elucidate the redox-reaction between $SrTiO_3$ and the Ti top electrode and to correlate it with the filament formation in the MIM structures and their electrical properties.

We investigated single crystalline thin films of the resistive switching model material $SrTiO_3$ (STO) with intentional Fe acceptor doping in order to prevent the influence of unintended background impurity acceptor doping. Thin films of 20 nm $SrTi_{1-x}Fe_xO_3$ (Fe:STO) with $x = 0.01$ and 0.05 were grown epitaxially on commercially available (001) oriented 1 at. % Nb-doped $SrTiO_3$ (Nb:STO) single crystals by pulsed laser deposition (PLD), using a KrF excimer-laser ($\lambda = 248$ nm), with an energy density of 0.8 J/cm^2, a frequency of 5 Hz and a substrate temperature of 700 °C at an oxygen pressure of 0.25 mbar (for more details, see Refs. 14 and 15). The Ti top electrodes capped with a 5 nm thick Pt layer were deposited by sequential sputtering and subsequently patterned by optical lithography into $20 \times 20\ \mu m^2$ electrodes with a distance of 5 μm and 1 μm for GISAXS and HAXPES, respectively. For electron spectroscopy and x-ray scattering experiments, samples with a thinner or no Pt capping layer were used.

The electrical characterization of Pt/Ti/Fe:STO/Nb:STO as well as Ti/Fe:STO/Nb:STO MIM structures (see sketch in Fig. 1(a)) was performed with an *Agilent B1500A* semiconductor analyzer. The influence of the Ti layer thickness on the initial resistance R_i of Pt/Ti/Fe:STO/Nb:STO samples is shown in Fig. 1(b). Samples with Ti electrodes of 3 and 5 nm thickness show significantly higher R_i compared to thicker electrodes. Due to the large scatter of the data, it is not possible to extract more details of the transition between the two types of samples from the measurements. We attribute the difference to a more effective reduction of the $SrTiO_3$ film by thick Ti electrodes. This is confirmed by the fact that MIM structures without Pt capping layer show a less pronounced reduction of R_i according to the preoxidation of the Ti electrodes by the surrounding atmosphere.

Resistive switching in eightwise polarity[7] with respect to the top electrode was observed for all Ti layer thicknesses. Fig. 1(c) shows typical current-voltage (I-V) curves of 3 different Ti top electrode thicknesses. For MIM structures with 3 nm Ti electrodes, which exhibit a high R_i, the first positive I-V branch (highlighted in red) deviates strongly from the later switching branches. This is an indication for an

a)S. Stille and Ch. Lenser contributed equally to this work.
b)Electronic mail: sebastian.stille@rwth-aachen.de.
c)Electronic mail: c.lenser@fz-juelich.de.

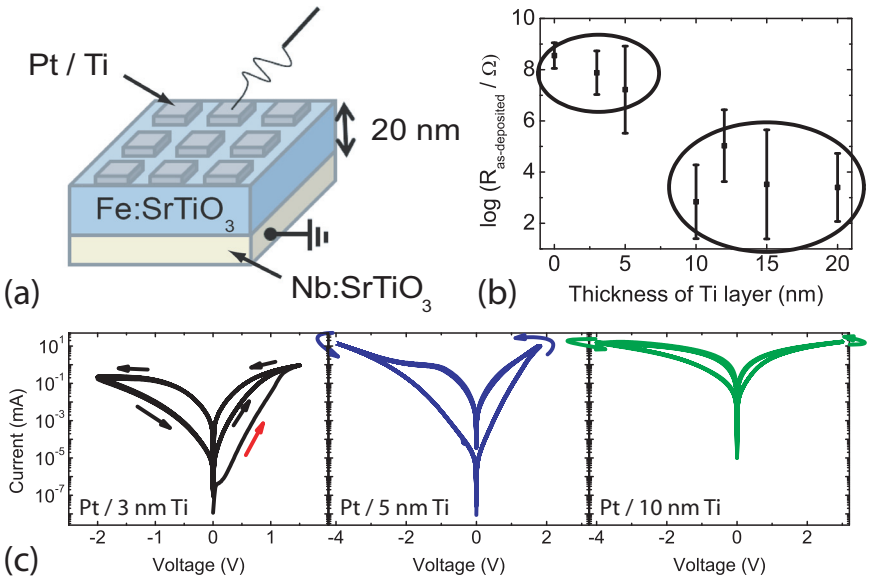

FIG. 1. (a) Sketch of the sample geometry. (b) Initial resistance of Pt/Ti/Fe:STO/Nb:STO MIM structures vs. thickness of Ti layer determined at ±100 mV. (c) Representative $I(V)$-curves of samples with different Ti thicknesses. Depending on the Ti thickness and the resulting initial resistivity, samples with Pt/Ti electrodes are forming-free.

irreversible forming step which occurs during the first application of a positive voltage. During this first sweep, oxygen is removed from the device and the samples are transformed to their low resistive state. For the MIM structures with thicker Ti layers, exhibiting a reduced R_i, the virgin sample is in the high resistive state and the first I-V cycle is already identical with the later switching cycles. Therefore, the samples can be regarded as forming-free. In particular, the forming behaviour is not primarily determined by the Ti thickness but by the resulting R_i. According to the large spread in the R_i depicted in Fig. 1(b), samples with 5 nm thick Ti electrodes are not generally forming-free. Furthermore, Fig. 1(c) nicely shows that the value of the high resistive state R_{OFF} decreases with the Ti thickness since it is identical with R_i, whereas the value of the low resistive state R_{ON} of all three types of samples is very similar. As a result, the R_{OFF}/R_{ON} ratio decreases with increasing Ti electrode thickness but can be as large as 10^3 for forming-free Pt/5 nm Ti electrodes. For samples with even lower R_i, the hysteresis in the I-V curve completely vanishes. In some cases, this type of highly conducting samples can be transformed into a switchable state by applying a forming step with negative polarity in order to remove oxygen vacancies from the Fe:STO thin film. In contrast to this strong influence of the Ti layer thickness, the electrode area shows no systematic influence on R_i and the switching behaviour. This is an indication that the Fe:STO thin film is reduced by the Ti top electrode in a rather filamentary than homogeneous way.

In order to elucidate chemical changes at the interface, which could be expected for oxidizing electrodes,[16,17] we performed HAXPES experiments at beamline P09 (HASYLAB, Hamburg), with an energy resolution of 500 meV as determined by the width of the Au Fermi-edge at a photon energy of $E_{photon} = 4200$ eV. For the spectra presented here, take-off angles close to the surface normal were chosen to maximize the information depth. We determined the effective attenuation length (EAL) in Pt and TiO_x to be 22 Å and 53 Å under these conditions, respectively.[18]

Figure 2 shows the Ti 2p photoemission spectra recorded on a 2 nm Pt/4 nm Ti/20 nm Fe:STO stack (bottom), as well as a 2 nm Pt/20 nm Fe:STO (middle) and a 5 nm Pt/100 nm Ti/Nb:STO sample (top) as references for the as-deposited Fe:STO and the Pt/Ti interface, respectively. We confirmed that the 2 nm Pt layer is closed by means of atomic force microscopy (AFM), LC-AFM, and SEM.[18] Only a single spin-orbit split doublet with the Ti $2p_{3/2}$ line at $E_{bind} = 458.9$ eV is observable for the Pt-covered Fe:STO, corresponding to Ti^{4+} and labelled as component A. The 5 nm Pt/100 nm Ti stack shows a Ti 2p spectrum that is dominated by metallic Ti (feature E at 454.1 eV), although some oxide is induced by surface oxidation and sample handling in air prior to measurements. The 2 nm Pt/4 nm Ti/20 nm Fe:STO stack shows a broad shoulder at the lower binding energy side of the Ti 2p doublet, while it is clear from the EAL values that we are probing the Ti/Fe:STO interface. We analyzed the envelope with a peak-fitting procedure assuming spectral components of Lorentzian lineshape with a FWHM of 1.5 eV for components B-D, although some Gaussian broadening of the peaks was permitted where it improved the fit. The envelope of the Ti 2p spectrum cannot be reproduced with less than four spectral

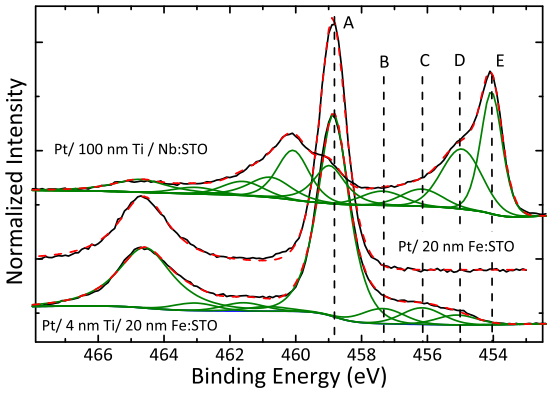

FIG. 2. Normalized Ti 2p spectra recorded on samples with and without a Ti layer, offset on the y-axis for clarity, and a 5 nm Pt/100 nm Ti stack. Black lines are measured data, while dashed red lines are the sum of the fitted spectral components (green lines). Features A-D can be assigned to different oxidation states of Ti (see text), while E indicates the presence of metallic Ti.

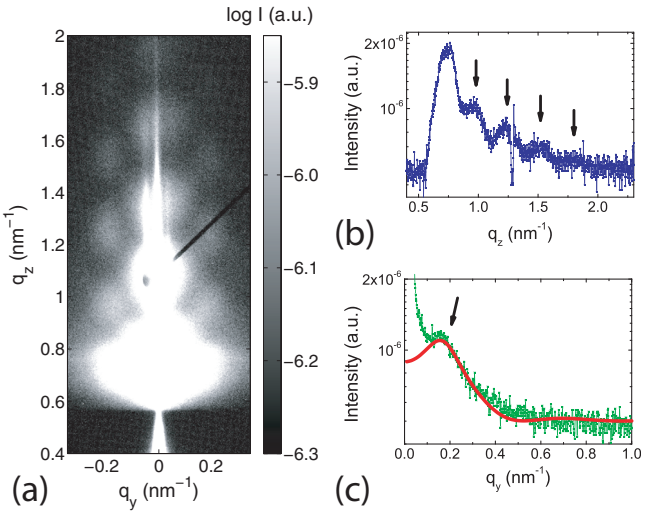

FIG. 3. (a) GISAXS pattern for sample 5 nm Ti/20 nm Fe:STO/Nb:STO. A laterally formed structure can be seen. (b) Vertical cut along $q_y = 0.2\,\mathrm{nm}^{-1}$. Arrows indicate oscillations. (c) Lateral cut along $q_z = 0.95\,\mathrm{nm}^{-1}$. Red line: Simulated GISAXS intensity with an arrow indicating a maximum.

components. According to their binding energy, component B (457.4 eV) and component D (455.1 eV) can be attributed to Ti_2O_3 and TiO, respectively.[19] The intermediate energy position of component C cannot be assigned to a specific oxidation state of Ti in a straightforward manner and likely corresponds to non-stoichiometric suboxides between TiO and Ti_2O_3, while metallic Ti is notably absent. From comparison with the reference samples, we conclude that the oxidation is mainly induced by the redox-reaction $Ti + SrTiO_3 \rightleftharpoons TiO_x + SrTiO_{3-x}$ with the underlying Fe:STO thin film. The resistance of the top electrode R_{TiO_x} remains low due to the presence of conductive Ti-suboxides; therefore $R_i = R_{TiO_x} + R_{STO}$ is high until a critical degree of reduction is reached in the STO film. The Ti layer acts as a sink for oxygen; therefore the redox-reaction can be shifted toward $TiO_x + SrTiO_{3-x}$ by increasing the Ti layer thickness or applying a voltage (compare Fig. 1). Since the reduction enthalpy is given by $-\Delta G_{STO} = -\Delta\bar{\mu} - zF\Delta\phi$, the Fe:STO can be reduced (or electroformed) prior to resistive switching by either an applied voltage ($V = \Delta\phi$) or a strong gradient in the chemical potential $\bar{\mu}$ (metal/oxide interface). In the above equation, z is the particle charge and F is the Faraday constant.

GISAXS experiments enable one to detect structural changes of thin films due to local differences in the electron density contrast.[20] GISAXS experiments on bare Fe:STO thin films and Fe:STO films with patterned arrays of Ti electrodes (area: $20\,\mu\mathrm{m} \times 20\,\mu\mathrm{m}$, distance: $5\,\mu\mathrm{m}$) were performed at beamline BW4 (HASYLAB, Hamburg).[21] While the Pt capping layer is beneficial for electrical characterization, the presence of a strong scatterer such as Pt suppresses most of the information obtainable through GISAXS from the lighter elements below. Therefore, Fe:STO thin films have been prepared without Pt capping layer. Cu marker structures were placed in-between those arrays in order to use the fluorescence signal to align the electrode arrays parallel to the x-ray beam.

Fig. 3(a) shows the resulting GISAXS pattern for an as-deposited 5 nm Ti/20 nm Fe:STO/Nb:STO sample. This structure has not been observed in a reference sample consisting of 20 nm Fe:STO/Nb:STO only and for samples with top electrodes consisting only of Pt. A vertical cut along $q_y = 0.2\,\mathrm{nm}^{-1}$ (Fig. 3(b)) shows the Yoneda peak at $q_z \approx 0.75\,\mathrm{nm}^{-1}$ followed by an oscillating intensity with a periodicity of $\Delta q_z = (0.29 \pm 0.03)\,\mathrm{nm}^{-1}$, from which the height of the scatterers can be calculated to be (21.7 ± 2.2) nm. This holds for both 5 and 15 nm Ti electrodes, and the observed structure is therefore connected to the 20 nm thick Fe:STO film.

A lateral cut along $q_z = 0.95\,\mathrm{nm}^{-1}$ (Fig. 3(c)) yields a correlation maximum for the observed pattern at $q_y \approx 0.152\,\mathrm{nm}^{-1}$. Simulations with the software FitGISAXS (Ref. 22) (red line in Fig. 3(c)) have been performed to obtain more quantitative information on the scatterers, which were modeled in a first approximation as cylinders with a different electron density compared to the surrounding STO film. The simulation of the off-plane (q_y) intensity was performed in a way that the correlation maximum (arrow in Fig. 3(c)) was reproduced as well as the right slope. The cylindrical form factor then yielded a mean cylinder diameter of $D \approx 15$ nm. The correlation peak gives a mean distance between the scatterers of $D' = 30$ nm. The region left to the correlation peak was not taken into account since it is dominated by in-plane scattering (cf. beam stop for the specular peak in Fig. 3(a)). It should be noted that the scattering pattern shown in Fig. 3(a) points to a filament geometry more complex than a simple cylinder. Nevertheless, the numerical values for the filament dimensions obtained in the cylinder approximation provide an estimate which compares well with the AFM measurements described below.

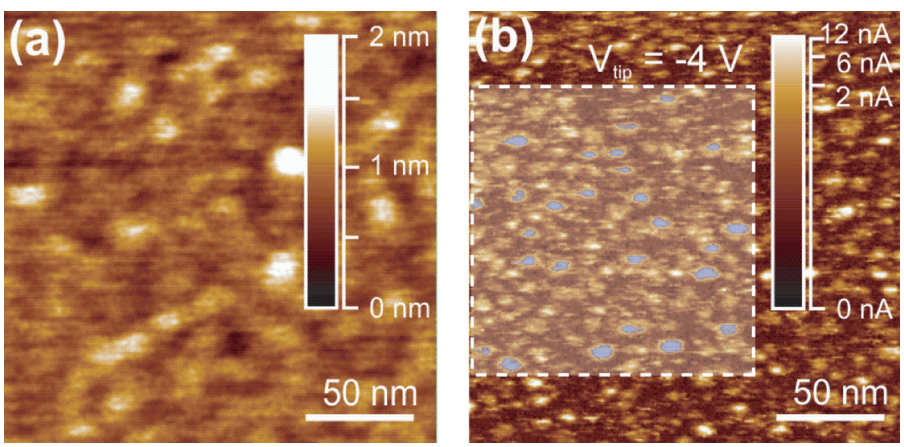

FIG. 4. AFM investigations of a Fe:STO thin film: (a) conductive AFM topography and (b) current scan of a 20 nm Fe:STO thin film on Nb:STO. The shaded area shows the part which has been considered for the statistical analysis of the conducting spots.

Fig. 4(b) shows a conductive tip AFM measurement (LC-AFM) of a Fe:STO thin film grown under the same conditions. After scanning, the surface of the film with a voltage of −4 V applied to the tip, which attracts oxygen vacancies to the sample surface,[23] it shows conducting spots embedded in an essentially insulating matrix. These spots can be identified with exits of conducting STO filaments on the thin film surface. According to our previous studies,[15] the positions of these filaments could be ascribed to defective thin film regions. According to the fact that the reduction enthalpy is lowered at extended defects in STO,[24] these areas are preferentially reduced by the application of the conductive tip. The shaded area in Fig. 4(b) was used to select spots for a statistical analysis. The selection of these spots has been carried out by using a threshold of 80% of maximum conductivity as well as a minimum value of the conductive area of 15 nm^2 (highlighted in blue). This reveals a mean diameter of the spots of 5 nm and a mean distance of 29 nm. It is interesting to note that the mean distance of these spots is very similar to the distance between the regions with increased electron density detected by GISAXS. However, the discrepancy between the spot diameter of the conducting spots and the filament diameter detected by GISAXS analysis might be explained by the fact that the filament exits at the surface might have a different diameter than the mean diameter underneath the surface. Whereas the conducting filaments in the LC-AFM experiment are formed by the tip-induced movement of oxygen vacancies, the filament formation beneath the Ti electrode is induced by the chemical gradient driven movement of oxygen vacancies. Certainly, this difference in the oxygen vacancy formation process could also result in a slightly different filament geometry.

Based on the above results, the following picture emerges: The inhomogeneities in the electron density detected by GISAXS can be considered as regions of the Fe:STO film where donor-type oxygen vacancies are induced by the redox-reaction with the Ti top electrode. The oxygen provided by the 20 nm thick Fe:STO thin films is sufficient to completely transform the metallic Ti top electrodes to a Ti sub-oxide as indicated by the shape of the Ti core levels (shown in Fig. 2). Driven by the chemical gradient, the amount of oxygen vacancies in the Fe:STO thin films and thereby the R_i is determined by the Ti electrode thickness as shown in Fig. 1(b).

In summary, we have shown that epitaxially grown 20 nm thick Fe:STO thin film devices with Ti top electrodes above a thickness of about 5 nm have a strongly reduced initial resistance, giving rise to forming-free devices. The detection of different Ti suboxides by HAXPES experiments proved a redox-process between the Ti top electrode and the Fe:STO thin film, which induces the increase of oxygen vacancies in the Fe:STO thin film. GISAXS investigations indicated the existence of scattering centers within the Fe:STO thin film with a mean distance of $D' = 30$ nm and a mean diameter of $D \approx 15$ nm using a cylindrical geometry in a first approximation. This can be attributed to a preferential reduction of defective thin film regions due to the lowered reduction enthalpy of extended defects in STO. As a result, the low resistive state of the forming-free devices consists of a preformed arrangement of oxygen deficient STO filaments, which give rise to a filamentary switching scenario.

This work has been supported in parts by the Deutsche Forschungsgemeinschaft (SFB 917) and by the NRW-EU Ziel 2-Programm (MATERA project FMRSM). The authors would like to thank HASYLAB for support and the beamline staff at P09 for their assistance, as well as C. S. Fadley for the measurements performed on reference samples. We are grateful to R. de Souza for helpful discussions.

[1]R. Waser and M. Aono, Nature Mater. **6**, 833 (2007).
[2]R. Waser, R. Dittmann, G. Staikov, and K. Szot, Adv. Mater. **21**, 2632 (2009).
[3]M. J. Lee, C. B. Lee, D. Lee, S. R. Lee, M. Chang, J. H. Hur, Y. B. Kim, C. J. Kim, D. H. Seo, S. Seo, U. I. Chung, I. K. Yoo, and K. Kim, Nature Mater. **10**, 625 (2011).
[4]D. B. Strukov, G. S. Snider, D. R. Stewart, and R. S. Williams, Nature **453**, 80 (2008).
[5]J. P. Strachan, J. J. Yang, R. Muenstermann, A. Scholl, G. Medeiros-Ribeiro, D. R. Stewart, and R. S. Williams, Nanotechnology **20**, 485701 (2009).
[6]R. Muenstermann, J. J. Yang, J. P. Strachan, G. Medeiros-Ribeiro, R. Dittmann, and R. Waser, Phys. Status Solidi (RRL) **4**, 16 (2010).
[7]R. Muenstermann, T. Menke, R. Dittmann, and R. Waser, Adv. Mater. **22**, 4819 (2010).
[8]X. Tran, B. Gao, J. Kang, X. Wu, L. Wu, Z. Fang, Z. Wang, K. L. Pey, Y. C. Yeo, A. Y. Du, M. Liu, B. Y. Nguyen, M. F. Li, and H. Y. Yu, in *IEDM Proceedings* (IEEE International, 2011), p. 713.
[9]X. Wu, Z. Fang, K. Li, M. Bosman, N. Raghavan, X. Li, H. Y. Yu, N. Singh, G. Q. Lo, X. X. Zhang, and K. L. Pey, Appl. Phys. Lett. **99**, 133504 (2011).
[10]Y. S. Chen, H. Y. Lee, P. S. Chen, T. Y. Wu, C. C. Wang, P. J. Tzeng, F. Chen, M. J. Tsai, and C. Lien, IEEE Electron Device Lett. **31**, 1473 (2010).
[11]C. Hermes, R. Bruchhaus, and R. Waser, IEEE Electron Device Lett. **32**, 1588 (2011).
[12]W. Wang, S. Fujita, and S. Wong, IEEE Electron Device Lett. **30**, 763 (2009).
[13]F. Nardi, D. Ielmini, C. Cagli, S. Spiga, M. Fanciulli, L. Goux, and D. J. Wouters, Solid-State Electron. **58**, 42 (2011).
[14]T. Menke, R. Dittmann, P. Meuffels, K. Szot, and R. Waser, J. Appl. Phys. **106**, 114507 (2009).
[15]R. Muenstermann, T. Menke, R. Dittmann, S. Mi, C.-L. Jia, D. Park, and J. Mayer, J. Appl. Phys. **108**, 124504 (2010).
[16]J. J. Yang, J. P. Strachan, F. Miao, M. Zhang, M. D. Pickett, W. Yi, D. A. A. Ohlberg, G. Medeiros-Ribeiro, and R. S. Williams, Appl. Phys. A: Mater. Sci. Process. **102**, 785 (2011).
[17]V. V. Afanas'ev, A. Stesmans, L. Pantisano, S. Cimino, C. Adelmann, L. Goux, Y. Y. Chen, J. A. Kittl, D. Wouters, and M. Jurczak, Appl. Phys. Lett. **98**, 132901 (2011).
[18]See supplementary material at http://dx.doi.org/10.1063/1.4724108 for information on the EAL and AFM and SEM investigations showing a closed Pt layer.
[19]A. Carley, P. Chalker, J. Riviere, and M. Roberts, J. Chem. Soc., Faraday Trans. **83**, 351 (1987).
[20]G. Renaud, R. Lazzari, and F. Leroy, Surf. Sci. Rep. **64**, 255 (2019).
[21]S. V. Roth, R. Doehrmann, M. Dommach, M. Kuhlmann, I. Kroeger, R. Gehrke, H. Walter, C. Schroer, B. Lengeler, and P. Mueller-Buschbaum, Rev. Sci. Instrum. **77**, 085106 (2006).
[22]D. Babonneau, J. Appl. Crystallogr. **43**, 929 (2010).
[23]K. Szot, W. Speier, G. Bihlmayer, and R. Waser, Nature Mater. **5**, 312 (2006).
[24]R. A. de Souza, Phys. Chem. Chem. Phys. **11**, 9939 (2009).